Published in final edited form as:

J Neurosci Methods. 2016 July 15; 267: 132–140. doi:10.1016/j.jneumeth.2016.04.014.

Design and Characterization of a Microfabricated Hydrogen Clearance Blood Flow Sensor

Lindsay R. Walton[a], **Martin A. Edwards**[a,1], **Gregory S. McCarty**[b], and **R. Mark Wightman**[a,c]

Lindsay R. Walton: waltonlr@email.unc.edu; Martin A. Edwards: martin.edwards@utah.edu; Gregory S. McCarty: gsmccart@ncsu.edu; R. Mark Wightman: rmw@unc.edu

[a]Department of Chemistry, University of North Carolina at Chapel Hill, Chapel Hill, NC, USA

[b]Department of Chemistry, North Carolina State University, Raleigh, NC, USA

[c]Neuroscience Center, University of North Carolina at Chapel Hill, Chapel Hill, NC, USA

Abstract

Background—Modern cerebral blood flow (CBF) detection favors the use of either optical technologies that are limited to cortical brain regions, or expensive magnetic resonance. Decades ago, inhalation gas clearance was the choice method of quantifying CBF, but this suffered from poor temporal resolution. Electrolytic H_2 clearance (EHC) generates and collects gas in situ at an electrode pair, which improves temporal resolution, but the probe size has prohibited meaningful subcortical use.

New Method—We microfabricated EHC electrodes to an order of magnitude smaller than those existing, on the scale of 100 μm, to permit use deep within the brain.

Results—Novel EHC probes were fabricated. The devices offered exceptional signal-to-noise, achieved high collection efficiencies (40 – 50%) in vitro, and agreed with theoretical modeling. An in vitro chemical reaction model was used to confirm that our devices detected flow rates higher than those expected physiologically. Computational modeling that incorporated realistic noise levels demonstrated devices would be sensitive to physiological CBF rates.

Comparison with Existing Method—The reduced size of our arrays makes them suitable for subcortical EHC measurements, as opposed to the larger, existing EHC electrodes that would cause substantial tissue damage. Our array can collect multiple CBF measurements per minute, and can thus resolve physiological changes occurring on a shorter timescale than existing gas clearance measurements.

Conclusion—We present and characterize microfabricated EHC electrodes and an accompanying theoretical model to interpret acquired data. Microfabrication allows for the high-

Corresponding Author: Dr. RM Wightman, Department of Chemistry and Neuroscience Center, Campus Box 3290, Caudill and Kenan Laboratories, University of North Carolina at Chapel Hill, Chapel Hill, NC 27599, USA. ; Email: rmw@unc.edu Phone: +1 919 962 1472

[1]Present address: Department of Chemistry, University of Utah, Salt Lake City, UT, USA.

throughput production of reproducible devices that are capable of monitoring deep brain CBF with sub-minute resolution.

Keywords

COMSOL Multiphysics; Electrolysis; Gas clearance; Photolithography; Platinum electrode

1. INTRODUCTION

Cerebral blood flow (CBF) increases in activated brain regions to deliver energy in the forms of glucose and O_2 – a phenomenon known as functional hyperemia.[1–3] This increase also serves to maintain non-cytotoxic levels of metabolic products and conserve physiological pH following neuronal activity. Disease states such as ischemia can dysregulate hyperemia and generate or perpetuate brain damage, as neurons become both deprived of energy substrates and exposed to toxic levels of neurotransmitters and metabolic products.[2–4] Beneath the cerebral cortex, densely packed capillaries fine-tune CBF activity to maintain homeostasis.[1, 3] A broad literature exists studying cortical CBF[5–7], but studying microvasculature control in the deep brain can provide new insight into pathologies hallmarked by CBF dysregulation, as well as flow activity in the behaving brain.

Numerous techniques have been used to measure CBF, including optical methods and tracer clearance approaches.[8–12] Laser Doppler flowmetry and laser speckle imaging are the most popular optical techniques, but the size of commercially available probes (500 μm or greater in diameter) risks extensive tissue damage to areas below the cortical surface.[6, 8, 13] Clearance techniques, which rely on detecting the transport of an inert tracer to quantify flow, can measure CBF throughout the brain. However, these methods are costly (e.g. magnetic resonance imaging) and/or have a finite number of measurements per animal dictated by the number of unique labels available (e.g. fluorescent tags for microspheres).[11, 14] Sensitivity to motion artifacts further excludes the most commonly used techniques, optical and magnetic resonance imaging, from CBF measurements in behaving subjects. As an increasing number of common anesthetics (e.g. isofluorane) are known to have vasoactive effects[15–17], development of a technique capable of exploring deep within the brain during conscious activity is highly desired.

Inert gases are attractive clearance tracers in biological subjects, as gas clearance can make an unlimited number of measurements per subject, detect CBF below the cortex, and perform in both anesthetized and freely-moving animals, all while quantifying CBF in ways that correlate highly with values obtained from competing techniques.[12, 18–23] The most affordable clearance gas is H_2, introduced through inhalation, injection of H_2-saturated saline, or electrolytic generation.[21, 24, 25] The lattermost, electrolytic H_2 clearance (EHC), generates H_2 *in situ* and monitors its clearance to measure blood flow. Using a collector-generator electrode array, inert H_2 is generated galvanostatically from endogenous water and reoxidized at a potentiostatic collector electrode. Common biological interferents oxidize at higher potentials than H_2, so a low collector potential ensures specificity for *in vivo* use.[25] Inhalation and injection H_2 clearance methods have poor temporal resolution, as gas takes minutes to permeate through tissues and saturate the brain for a single measurement[23, 26],

whereas EHC generates gas locally and reduces saturation time to seconds.[24, 27] However, existing EHC electrodes are a millimeter or larger in diameter, too large for anything other than superficial CBF measurements.[20, 24, 27] Despite its superior temporal resolution, EHC has not been used for CBF detection in subcortical, freely-moving experiments due to the technical limitations of probe size.

In this paper we use photolithography to fabricate a platinum electrode array capable of EHC that is an order of magnitude smaller than previous sensors.[24, 27] Micron-scale dimensions improve spatial resolution and allow for sub-surface CBF measuring with minimal tissue damage. Microfabricated EHC fulfills the need for a tool capable of measuring CBF in the deep brain on a more physiological timescale than existing gas clearance methods, with the crucial benefit of applicability during freely-behaving experiments. Here, we characterize our EHC array, assess its suitability as a blood flow sensor, and present a theoretical framework for analyzing the data it produces.

2. EXPERIMENTAL

2.1. Chemicals and Solutions

Chemicals were received from Sigma Aldrich (St. Louis, MO) unless otherwise noted. Phosphate buffered saline (PBS, 140 mM NaCl, 3 mM KCl, 10 mM NaH_2PO_4) was diluted from a 10× stock and adjusted to pH = 7.4 with 5 M NaOH on the day of use. Hexaammineruthenium (III) trichloride (RuHex) was dissolved in 0.1 M KCl. McIlvaine buffers were made on the day of use from 0.1 M citric acid and 0.2 M K_2HPO_4, according to the pH value desired. DL-Noradrenaline hydrochloride (norepinephrine, NE) was added to buffer immediately prior to collecting rate data. All solutions were at 25 °C.

2.2. Platinum Electrode Array Fabrication

Platinum EHC arrays (Figure 1A) were fabricated using instruments at both the North Carolina State University Nanofabrication Facility (NNF) and the Chapel Hill Analytical and Nanofabrication Laboratory (CHANL) at UNC Chapel Hill. The process used was similar to arrays that we previously reported.[28] Silicon wafers (University Wafer, Inc., Boston MA) were insulated with silicon nitride (3000 Å) using low-pressure chemical vapor deposition (LPCVD). Photolithography was performed using a negative tone photoresist (NFR 016 D2, JSR Corp., Tokyo, Japan) following dynamic application of hexamethyldisilazane (HMDS) as an adhesion promoter to obtain a thickness of approximately 3.7 μm. After exposure and development of the photoresist, the nitride was dry-etched using reactive ion etching (RIE) to pattern trenches of approximately 600 Å. Titanium metal was evaporated over the entire wafer (200 Å) to aid adhesion between the LPCVD nitride and subsequently evaporated platinum (400 Å). Lift-off was achieved with acetone, followed by a standard RCA-1 clean.

The arrays were insulated with silicon nitride (3000 Å) using plasma-enhanced chemical vapor deposition (PECVD). Photolithography using HMDS followed by S1813 positive tone photoresist (Shipley, Marlborough, MA) isolated areas of electrical exposure. The PECVD nitride was dry-etched through to the LPCVD nitride. A thick (>10 μm), protective layer of

positive photoresist (AZ 4620, Shipley) was spun atop the wafer. Each wafer totaled 81 individual devices with different array dimensions, 26 of which were the geometry described in this paper. Devices were ultimately isolated using a dicing saw. Electrical connections to contact pads were made manually under a microscope using stainless steel wire and silver epoxy (MG Chemicals, Canada). Platinum devices were cleaned via voltammetric cycling in 0.5 M H_2SO_4 and were excluded from the study if the steady state current measured by slow-scan voltammetry in quiescent RuHex solution was not in agreement with that predicted by theory (finite element simulations). Platinum black coatings were applied to 3 devices, as previously described[29], to increase electrochemically active surface area. Carbon arrays used for cyclization experiments were previously fabricated in the laboratory and had the same dimensions as the platinum devices used in this paper.[28]

2.3. Data Acquisition

Custom hardware was assembled (UNC Chemistry Electronics Shop, Chapel Hill, NC) for galvanostatic control of the generator electrode. Voltammetry data was collected with a Chem-Clamp potentiostat (Dagan Corporation, Minneapolis, MN) and filtered at 100 Hz. Carbon disk measurements were made using an EI-400 potentiostat (Ensman Instruments, Bloomington, IN). All data were acquired using custom, locally written LabVIEW (National Instruments, Austin, TX) programs with 60 Hz collection frequency. A Ag/AgCl wire reference was used and potentials reported herein are relative to this electrode. Galvanostatic generation was used to ensure consistent H_2 production regardless of electrode fouling or surface changes that could affect the voltage response. Generator currents were −100 nA unless otherwise noted. The collector potential was held at +0.25 V. Between each galvanostatic pulse, the collector electrode was cycled briefly (2–4 s, 20 V s^{-1}, from −0.5 V to +1.0 V) to maintain platinum surface integrity and collector current reproducibility.

2.4. Norepinephrine Cyclization Experiments

The rate of the cyclization of NE-orthoquinone (the oxidation product of NE) to leuco-noradrenochrome was used to assess the suitability of the devices for detecting flow rates, using an experimental paradigm akin to that used in clearance data. Electrode arrays of identical geometry to the platinum electrode array, but with carbon electrodes, were used. The collector was held at 0.0 V, and the generator used 10 s, +100 nA pulses to oxidize NE to NE-orthoquinone. Data were acquired in McIlvaine buffers of varying pH (7.40 – 8.05) before and after the addition of 100 μM NE.

The rate of cyclization in solutions of the same pH range was independently measured using potential step chronoamperometry at a glassy carbon disk (r = 1.5 mm) collected at 60 Hz. The electrode was polished for 30 s with a 0.05 μm alumina slurry, rinsed with methanol and deionized H_2O, and sonicated for 1 minute between each data collection to maintain consistency.[30] Rates of cyclization for each pH were calculated as previously described.[31]

2.5. Modeling

Finite element modeling was used to calculate the spatially varying H_2 concentration over time. At time $T = 0$ the current at the generator was stepped from zero, i.e., no electrochemical reaction occurring, to a cathodic current, i_{gen} (taken to be negative in the

following discussion), achieving the reduction reaction in Equation 1. At time T^*, the current returns to zero.

$$2H^+ + 2e^- \rightarrow H_2 \quad (1)$$

The initial concentration of H_2 was taken to be to be zero throughout the simulation domain. Mass transport was described by the time-dependent version of the reaction-diffusion Equation 2, which is solved in the three dimensions; X, Y and Z.

$$\frac{\partial C}{\partial T} = D\nabla^2 C - KC \quad (2)$$

C represents the concentration of H_2, $D = 5\times10^{-5}$ cm^2s^{-1} its diffusion coefficient[32], T the time (s), and K (s^{-1}) the first order rate constant H_2 clearance, as proposed by Stosseck et al.[24, 25]

The boundary condition for the generator electrode is

$$D\nabla C \cdot \text{áźĽ} = \frac{i_{\text{gen}}(T)}{2AF} \quad (3)$$

where

$$i_{\text{gen}}(T) = \begin{cases} i_{\text{gen}} & \forall 0 \le T \le T^* \\ 0 & \forall T < 0 \text{ and } T > T^* \end{cases} \quad (4)$$

In these equations, $\underline{n}$ is the inward pointing unit normal, F is Faraday's constant and A is the generator electrode area. The factor of 2 arises from Equation 1 stoichiometry. Uniform surface flux is assumed, as the reaction is kinetically limited within the current range investigated. Implicit in this description is the assumption that all of the current is consumed by the evolution of H_2 (Equation 1) and that generated H_2 adsorption to the surface is negligible.[32]

The insulating parts of the array are described by

$$\nabla C \cdot \text{áźĽ} = 0 \quad (5)$$

and the exterior of the domain is taken to have zero concentration of H_2, that is

$$C = 0 \quad (6)$$

The collector electrode potential is set such that the reverse reaction of Equation 1 occurs at a diffusion-limited rate and is also described by Equation 6 The current at the collector, i_{coll}, is an integral of the flux computed over the surface of the electrode,

$$i_{\text{coll}} = 2D\int \nabla C \cdot \text{áźĽ} \quad (7)$$

where the 2 comes from the stoichiometry in Equation 1.

To reduce the number of degrees of freedom we normalized the equations in time, length and concentration by making the following substitutions

$$t=\frac{T}{\tau} \text{ where } \tau=\frac{a^2}{D} \quad (8)$$

$$x=\frac{X}{a};y=\frac{Y}{a};z=\frac{Z}{a} \quad (9)$$

$$c=C/\chi \text{ where } \chi=-i_{\text{gen}}\frac{a}{2AFD} \quad (10)$$

Where *a* is a characteristic length from the geometry, which in our case was taken to be the width of the collector electrode. This leads to the normalized version of Equation 2:

$$\frac{\partial c}{\partial t}=\nabla^2 c-kc \quad (11)$$

with the normalized rate constant *k* defined as

$$k=K\tau \quad (12)$$

and a modified set of boundary conditions

$$\nabla c\cdot \acute{a}\acute{z}\text{Ł}=-1 \quad \forall 0\le t\le t^* \quad (13)$$

$$\nabla c\cdot \acute{a}\acute{z}\text{Ł}=0 \quad \forall t<0 \text{ and } t>t^*$$

$$\nabla c\cdot \acute{a}\acute{z}\text{Ł}=0 \quad (14)$$

$$c=0 \quad (15)$$

that are the normalized equivalents of Equations 3, 5, and 6 respectively, applying to the same boundaries in the transformed geometry, and $t^* = T^*/\tau$. Note, $\underline{n}$ is used here to represent the inward pointing unit normal in the transformed coordinates.

The i_{coll} in non-normalized coordinates is related to the normalized form, $\tilde{\imath}_{coll}$, by

$$i_{\text{coll}}(T)=Da\chi\tilde{\text{É}}\text{Ł}_{\text{coll}}(t) \quad (16)$$

$$\tilde{\text{É}}\text{Ł}_{\text{coll}}(t)=\int\nabla c(t)\cdot \acute{a}\acute{z}\text{Ł}$$

where the integration is taken over the electrode in the normalized coordinates.

We made the useful observation that Equation 11 displays linearity; that is, if both $c_1(t)$ and $c_2(t)$ are linear then $c_3(t) = d_1c_1(t) + d_2c_2(t)$ will also be linear for any values d_1 and d_2. This property arises from the first order clearance rate description and is not true for general clearance expressions. We also observe that Equation 11 is time invariant, meaning $c_4(t) = c_1(t + t_0)$ is also a solution for any value of t_0.

If we define $c_\infty(t)$ as the solution for an infinitely long current pulse, initiated at $t = 0$, then we can derive the solution for a pulse of duration t^*, also initiated at $t = 0$, is described by

$$c_{t^*}(t) = c_\infty(t) - c_\infty(t - t^*) \quad (17)$$

Equation 11 is satisfied by the linearity relation ($d_1 = 1$, $d_2 = -1$) and time invariance ($t_0 = t^*$). Boundary conditions 14 and 15 are trivially satisfied and 13 is satisfied by the summation of the fluxes, which cancel out for $t > t^*$. The current is similarly given by

$$\tilde{I}_{\mathrm{coll},t^*}(t) = \tilde{I}_{\mathrm{coll},\infty}(t) - \tilde{I}_{\mathrm{coll},\infty}(t - t^*) \quad (18)$$

Where $\tilde{\imath}_{coll,t}$ and $\tilde{\imath}_{coll,\infty}$ represent the normalized collector current for a current pulse of duration t^* and infinite length, respectively. Thus we can restrict ourselves to solving these equations for an infinite pulse length, in practice until a (quasi) steady-state behavior is reached, for a range of geometries in the normalized space.

2.6. Computational Details

The solution to the equations was calculated using the commercial finite element modeling package COMSOL Multiphysics 4.3a (COMSOL AB) and was performed on the Biomedical Analysis and Simulation Supercomputer (BASS) at UNC Chapel Hill. The equations were discretized using a mesh which was chosen to be finest around the edge of the electrodes where flux is greatest. The mesh was determined to be sufficiently fine when further refinements did not perturb the solution. Similarly, the extent of the domain was made sufficiently large such that it did not affect the derived solution.

2.7. Simulated Flow Rate Analysis

Noise (0.02 – 0.4 nA) was added to simulated data at all flow rates, including 0 s^{-1}, in the form of normally distributed, random numbers with a zero mean. This process was repeated 5 times for each noise amplitude to determine the variation of the observed response. When performing analysis, data from 0 – 8 s was disregarded to exclude the generating pulse time and the first second of clearance and analyzed according to Stosseck et al (*vide infra*).[24] Statistical work was performed in GraphPad Prism 6 (GraphPad Software, San Diego, CA, USA). Student's *t*-tests were used to determine significance, defined as $P < 0.05$.

3. RESULTS

EHC arrays consisting of two individually addressable platinum electrodes were microfabricated (Figure 1A). The platinum is electrically insulated beneath silicon nitride, with the exception of two pads at the top that connect to either the potentiostat or galvanostat, and a window at the tapered tip that exposes band electrodes where EHC is

performed (Figure 1A, inset). The total probe width at the active electrode window is 100 μm, an order of magnitude smaller than existing EHC probes and more similar to existing microfabricated arrays used *in vivo*.[24, 33] The electrically insulated region between each electrode is approximately 5 μm wide. We used the two outer bands, each 100 × 20 μm, as the generator and the center electrode, 100 × 10 μm, as the collector. While exchanging the choice of the generator and collector would result in a higher overall collection efficiency (CE), defined as the percentage of the generator current measured at the collector electrode, the smaller generator area decreases the maximum current that could be applied and offers no signal enhancement. Higher current densities risk limiting the electrode lifespan or generating H_2 bubbles.[24, 34] Of the isolated, diced devices from two separately processed wafers, 42 / 52 (80.8%) were functional, 6 / 52 (11.5%) were excluded (criteria for exclusion *vide supra*), and 4 / 52 (7.7%) could not have functionality assessed due to human error.

3.1. Characterizing Platinum Arrays

The one-electron reduction of RuHex (III) to RuHex (II) is an outer-sphere redox system with fast electron transfer kinetics that is ideal for characterizing microelectrodes. To validate that the electrodes had been correctly produced, cyclic voltammetry was performed at 5 mV s^{-1} in degassed 2.5 mM RuHex (III) solutions to obtain steady state currents (i_{ss}). Background subtracted voltammogram currents show excellent agreement with simulation-calculated i_{ss} values (D = 9×10^{-6} cm^2s^{-1}, Figure 1B, dashed lines).[35]

RuHex (III) reduction at the generator served as a model system to compare experimental clearance curves to those calculated. A current pulse (i_{gen} = −100 nA) reduced RuHex (III) to RuHex (II). This current is within the kinetically controlled current regime of a 35 mM solution (i_{ss} = −578.5 nA at the generator) to eliminate the possibility of reducing other species (e.g. O_2). The current at the collector, held at +0.25 V to re-oxidize Ru(II), shows excellent agreement with the response calculated from simulations matching the experimental conditions (Figure 1C).

The theoretical response was calculated with varying pulse durations. Simulations determined that a 10 s generator current pulse was sufficient to reach locally saturated current with an expected 41.3% CE. Experimental results were in good agreement with CEs of 37.4 ± 5.9% ($t_{(2,4)}$ = 1.478, $P > 0.05$, Figure 1D). If greater CE were required, coating all electrodes with platinum black was shown to increase electroactive surface area significantly as compared to bare platinum, enhancing experimental CE to 54.8 ± 2.2% ($t_{(2,6)}$ = 4.804, P = 0.003).[29]

Suggested size: 2-column fit

3.2. Hydrogen Generation and Clearance

EHC at bare platinum electrodes was first tested in an acidic solution, 0.5 M H_2SO_4, both because of its ability to clean platinum surfaces and for its availability of free protons. The electrodes were initially cycled between −0.5 and +1.0 V at 20 mV s^{-1} and verified as clean when the cyclic voltammograms at 20 V s^{-1} produced the classic peaks indicative of H_2 and O_2 adsorption and desorption (Figure 2A). The pulse time necessary to achieve steady-state

CE could be decreased to 7 s (Figure 2B), as H_2 has a larger diffusion coefficient than RuHex.

Table 1 summarizes CE values obtained from EHC experiments in various solutions. Solutions left open to air had 25.2 ± 3.0% CE (n = 5 devices, dashed line, Figure 2B), significantly poorer than theoretical predictions of 43.6% CE ($t_{(2,4)} = 13.71$, $P = 0.0001$, n = 5). When the solution was degassed, the decrease in O_2 was seen in the steady-state cyclic voltammograms as increased area beneath the H_2 adsorption-desorption peaks and diminished area beneath those of O_2 (Figure 2A). This is consistent with the idea that degassed solutions have less O_2 capable of adsorbing to, and thus partially passivating, the active area of a bare platinum surface.[36] The clearance response in degassed acid closely matched that predicted by simulation (black line vs. gray line, Figure 2B) and achieved 34.6 ± 5.9% CE ($t_{(2,3)} = 3.05$, $P > 0.05$, n = 4). Similarly, in solutions of aerated PBS, no collection current was obtained using $i_{gen} = -100$ nA, and $i_{gen} = -700$ nA pulse yielded only 0.49 ± 0.18% CE ($t_{(2,3)} = 479.0$, $P < 0.0001$, n = 4). Once degassed, 30.4 ± 7.4% CE could be achieved in PBS using $i_{gen} = -100$ nA ($t_{(2,2)} = 3.09$, $P > 0.05$, n = 3 devices).

Suggested size: 1 column width

The decrease in CE is due to an O_2-dependent competing reduction that consumes a large fraction of the generator current and produces one or more species that are undetectable amperometrically at +0.25 V. While this is problematic for *in vitro* studies in air-saturated solutions, O_2 concentrations in the deep brain are approximately 5 times lower (~50 μM vs. ~250 μM at pH 7.4, 25°C[37]), thus it is expected that a majority of the current would go into producing H_2 *in vivo*.[38, 39] It is important to note that the +0.25 V holding potential is sufficiently higher than the reduction potential of O_2 itself, in addition to being lower than the oxidation potentials of common biological interferents (e.g. H_2O_2, ascorbic acid), ensuring that *in vivo* measurements will be insensitive to fluctuations in these analytes and specific for H_2.[21, 25]

Another operational problem *in vitro* was a decrease in CE with consecutive pulses (Figure 2C). Cycling the collector between pulses (20 V s^{-1}, 2–4 s, −0.5 to +1.0 V) regained optimal CE and maintained reproducibility. We attribute this passivation to oxygen atom adsorption to the positively-polarized collector surface, which strips off with cycling.[40]

Suggested size: 1 column width.

3.3. Modeled Flow

Localized flow, termed microflow, can be determined from clearance curves following the procedures of Stosseck et al.[24] After reaching saturated values of H_2 as assessed by a stable collection current plateau, galvanostatic generation ceases and H_2 clearance through diffusion and microflow begins. Note that, as total electroactive array area is 100 μm × 60 μm and the average spacing between blood vessels is ~50 μm, clearance from a H_2-saturated tissue volume will incorporate flow from multiple blood vessels.[41]

Previous works have shown that the clearance curve, the monoexponential current decay following the cessation of the generator pulse, provides a more reliable prediction of

microflow than absolute current values achieved at saturation.[22] Current during clearance is expected to obey the following relation from Stosseck et al.

$$\ln\left(\frac{i_0}{i_F}\right)=Kt+b \quad (19)$$

where i_0 (nA) and i_F (nA) represent clearance currents in the absence and presence of flow, respectively, K (s^{-1}) is the microflow included in our model as a first-order rate (Equation 2), and b a constant deviation function.[24] For convenience, we take $t = 0$ in Equation 19 to be the time when the generator pulse ends. Note, inhalation clearance experiments using millimeter-scale electrodes have reported polyexponential clearance rates because diffusion between grey and white matters differ, but our probe is small enough that we expect to avoid this issue.[42]

Modeled clearance data were analyzed according to Equation 19 and plotted as $\ln(i_0/i_F)$ vs. t (Figure 3A). The first second of clearance data was disregarded as the current ratio was constant, ~1, and contains no microflow information. The linear regressions were fit to the data from $t = 1$–8 s (Figure 3A) to obtain K values as slopes, making the time of one full CBF measurement total ~15 s and vastly improving temporal resolution compared to the multiple minutes per measurement seen in inhalation H_2 clearance.[22, 23] Ideally, these slope values would match the microflow rates input into the simulations, but fitting the data during this time range overestimates the input rates by ~15%, seen as a deviation from unity of the slope comparing the input microflow rates to those obtained from the slope fit (Figure 3B). This deviation highlights the importance of theoretical validation and indicates that the assumptions within Equation 19 are not strictly true, especially for shorter times.[24] We conjecture that this deviation arises due to the strong concentration gradients between the two electrodes, which are an order of magnitude closer than those originally used.[24] Fitting clearance data to longer time lengths decreases the magnitude of microflow overestimation, however it lowers temporal resolution. Since the relationship between the theoretically predicted and actual flows is linear, actual microflow can be calculated using a conversion factor obtained from simulations that match experimental parameters. This clearance protocol and analysis outline was optimized to establish balance between temporal resolution and flow rate accuracy for our specific geometry. Different protocols can be used with similar analysis to achieve desired metrics.

As the *ln* ratio used in this simple EHC data analysis exaggerates differences in current, one must also consider the magnitude of these differences and the impact of noise on their calculation. Randomly generated Gaussian noise was added to the simulated currents and the data were reanalyzed according to Equation 19 (Figure 3C). Simulations were calculated with ~60 Hz time resolution to match experimental protocol. As expected, data analyzed with greater noise gave less reliable microflow values (Figure 3D). However, with experimentally achievable low noise levels (<0.05 nA in this case), calculated microflows show close agreement with expected values. The exact noise amplitude that ensures accuracy is a function of the array geometry and acquisition protocol (data not shown). In conclusion, finite element modeling faithfully reproduces the experimental phenomena and

can be used to optimize and assess the suitability of novel geometries, quantify the robustness to noise, and calculate calibration factors.

Suggested size: 1.5 column width

3.4. Detecting "Flow" with Microarrays

A first-order chemical reaction was used as an *in vitro* model amenable to use with our arrays, as clearance currents exhibit first-order exponential decay.[24] The conversion of NE-orthoquinone, the oxidized product of NE, to its cyclized form, leuco-noradrenochrome, was chosen, as the products are voltammetrically distinguishable and the reaction rate has been characterized. The rate of 0.98 ± 0.52 s^{-1} at pH 7.40[43] can be slowed by increasing the pH, necessary to better mimic the microflow rates expected for *in vivo* EHC (i.e. 0.005–0.030 s^{-1}).[44]

We initially assessed the cyclization rate at a range of pH values by stepping the potential at a polished glassy carbon electrode from −0.4 V to +0.5 V. The current-time response for each pH value was analyzed according to the time-dependent equation for an ECE process.[45] The cyclization rates obtained were plotted against their corresponding pH values to verify the expected linear relationship (Figure 4A, $R^2 = 0.79$). Calculated rates were between 0.37 s^{-1} at pH 8.13 and 0.70 s^{-1} at pH 7.40.

Carbon pyrolyzed photoresist film (PPF) collector-generator arrays were used to monitor the cyclization rate because their surfaces can be stripped of the cyclized product, known to foul electrodes, by scanning to high voltages.[46] Electrodes were assessed using cyclic voltammetry in solutions of 100 μM NE (Figure 4B). With 50 mV s^{-1} scan rates, NE is oxidized and reaches a diffusion-limited plateau at ~0.1 V. No reduction peak is observed on the reverse scan as there is sufficient time for the NE-orthoquinone to diffuse away. At 500 mV s^1, two reduction peaks are observed relating to NE-orthoquinone (Peak 1) and its cyclized form (leuco-noradrenochrome, Peak 2).[31]

For clearance measurements, generator electrodes oxidized NE (i_{gen} = +100 nA, 10 s) while the collector held 0.0 V; a potential sufficient to detect NE, but not the cyclized product (Figure 4B). In buffer, negligible changes to the collector current were detected (−0.04 ± 0.02 nA), confirming collection currents as being solely NE-orthoquinone. The 50 mV s^{-1} voltammogram i_{ss} shows that the complete oxidation of NE to NE-orthoquinone will consume 2–3 nA, thus we can be confident that the same diffusion-limited quantity is generated in all experiments. Voltage at the generator greatly exceeded that required to completely oxidize NE in our solutions (Figure 4C).

In solutions within the pH range studied, a non-zero i_{ss} was achieved within 5 s (−0.54 ± 0.05 nA, −0.74 ± 0.08 nA, −1.00 ± 0.13 nA, for pH 7.62, 7.83, 8.05, respectively), indicating that a portion of the oxidized product was not cyclized (Figure 4D). Higher collector currents at higher pH values are consistent with cyclization rates slowing under increasingly basic conditions. It is impossible to slow the reaction rate to zero to perform a $\ln(i_0/i_F)$ analysis, however, the variation in current indicates the ability of the array to sense reduced NE-orthoquinone before an intracyclization process that occurs at rates between

0.37 – 0.70 s^{-1}. This experimental demonstration coupled with the previous theoretical results demonstrate the feasibility of performing measurements over a wide range of microflow rates, including those expected for CBF.

An important observation from these data is that the noise in the current collector is 0.02 ± 0.009 nA, below the 0.05 nA maximum noise for accurate determination of CBF (*vide supra*). This justifies the previously made assertion that we may use these devices to measure CBF. We conclude that our chosen geometry is capable of discerning microflow for rates at least as low as 0.005 s^{-1} and as high as 0.70 s^{-1}, which is well above what is to be expected *in vivo*.

Suggested size: 1.5 column width

4. CONCLUSIONS

We report microfabricated EHC electrodes that are capable of detecting and reliably quantifying changes in CBF expected *in vivo*. Finite element modeling accurately reproduces the experimental current and allows us to calculate calibration factors, quantify the effect of noise, and choose optimized geometries and protocols. Microfabrication, which allows batch fabrication of implantable sensors in reproducible yields of >80%, enables EHC arrays to be a more affordable alternative to existing CBF detection techniques. These devices have high temporal and spatial resolution, and implanting an electrode ensures its insensitivity to subject motion. These advantages over both traditional EHC sensors and other CBF measuring techniques importantly present opportunities for future experiments where *in vivo* CBF quantification can take place in freely-moving subjects beneath the cortex.

Acknowledgments

This research was achieved with financial support from NIH (DA 032530). BASS work was made possible with NIH grant 1S10RR023069-01. The authors acknowledge Dr. Adam Dengler for donating carbon arrays used in the cyclization experiments; Marcio Cerullo, Bruce Sprague, and Henry Taylor at the NNF and Bob Geil at CHANL for microfabrication assistance; and Meg Fox for her careful reading of this manuscript and insightful comments. They are grateful for the homemade galvanostat used for all clearance data, courtesy of Collin McKinney from the UNC Electronics Shop.

References

1. Attwell D, Buchan AM, Charpak S, Lauritzen M, MacVicar BA, Newman EA. Glial and neuronal control of brain blood flow. Nature. 2010; 468:232–243. [PubMed: 21068832]
2. Haydon PG, Carmignoto G. Astrocyte control of synaptic transmission and neurovascular coupling. Physiol. Rev. 2006; 86:1009–1031. [PubMed: 16816144]
3. Iadecola C. Neurovascular regulation in the normal brain and in Alzheimer's disease. Nat. Rev. Neurosci. 2004; 5:347–360. [PubMed: 15100718]
4. Hossmann KA. Viability thresholds and the penumbra of focal ischemia. Ann. Neurol. 1994; 36:557–565. [PubMed: 7944288]
5. Harper AM, Glass H. Effect of alterations in the arterial carbon dioxide tension on the blood flow through the cerebral cortex at normal and low arterial blood pressures. J. Neurol. Neurosurg. Psychiatry. 1965; 28:449. [PubMed: 5838479]

6. Dirnagl U, Kaplan B, Jacewicz M, Pulsinelli W. Continuous measurement of cerebral cortical blood flow by laser-Doppler flowmetry in a rat stroke model. J. Cereb. Blood Flow Metab. 1989; 9:589–596. [PubMed: 2674168]
7. Takano T, Tian G-F, Peng W, Lou N, Libionka W, Han X, et al. Astrocyte-mediated control of cerebral blood flow. Nat. Neurosci. 2006; 9:260–267. [PubMed: 16388306]
8. Shih AY, Driscoll JD, Drew PJ, Nishimura N, Schaffer CB, Kleinfeld D. Two-photon microscopy as a tool to study blood flow and neurovascular coupling in the rodent brain. J. Cereb. Blood Flow Metab. 2012; 32:1277–1309. [PubMed: 22293983]
9. Boas DA, Dunn AK. Laser speckle contrast imaging in biomedical optics. J. Biomed. Opt. 2010; 15 011109-011109-12.
10. Ter-Pogossian MM, Eichling JO, Davis DO, Welch MJ. The measure in vivo of regional cerebral oxygen utilization by means of oxyhemoglobin labeled with radioactive oxygen-15. J. Clin. Invest. 1970; 49:381. [PubMed: 5411789]
11. Prinzen FW, Bassingthwaighte JB. Blood flow distributions by microsphere deposition methods. Cardiovasc. Res. 2000; 45:13–21. [PubMed: 10728307]
12. Kety SS. The theory and applications of the exchange of inert gas at the lungs and tissues. Pharmacol. Rev. 1951; 3:1–41. [PubMed: 14833874]
13. Dunn AK, Bolay H, Moskowitz MA, Boas DA. Dynamic imaging of cerebral blood flow using laser speckle. J. Cereb. Blood Flow Metab. 2001; 21:195–201. [PubMed: 11295873]
14. Edvinsson, L.; Krause, DN. Cerebral Blood Flow and Metabolism. Lippincott Williams & Wilkins; 2002.
15. Ueki M, Mies G, Hossmann KA. Effect of alpha-chloralose, halothane, pentobarbital and nitrous oxide anesthesia on metabolic coupling in somatosensory cortex of rat. Acta Anaesthesiol. Scand. 1992; 36:318–322. [PubMed: 1595336]
16. Lindauer U, Villringer A, Dirnagl U. Characterization of CBF response to somatosensory stimulation: model and influence of anesthetics. Am. J. Physiol. Heart Circ. Physiol. 1993; 264:H1223–H1228.
17. Matta BF, Heath KJ, Tipping K, Summors AC. Direct cerebral vasodilatory effects of sevoflurane and isoflurane. Anesthesiology. 1999; 91:677–677. [PubMed: 10485778]
18. Pell GS, King MD, Proctor E, Thomas DL, Lythgoe MF, Gadian DG, et al. Comparative study of the FAIR technique of perfusion quantification with the hydrogen clearance method. J. Cereb. Blood Flow Metab. 2003; 23:689–699. [PubMed: 12796717]
19. Machens HG, Pallua N, Mailaender P, Pasel J, Frank KH, Reimer R, et al. Measurements of tissue blood flow by the hydrogen clearance technique (HCT): A comparative study including laser Doppler flowmetry (LDF) and the erlangen micro-lightguide spectrophotometer (EMPHO). Microsurgery. 1995; 16:808–817. [PubMed: 8844663]
20. DiResta G, Kiel J, Riedel G, Kaplan P, Shepherd A. Hybrid blood flow probe for simultaneous H2 clearance and laser-Doppler velocimetry. Am. J. Physiol. Gastrointest. Liver Physiol. 1987; 253:G573–G581.
21. Aukland K, Bower BF, Berliner RW. Measurement of local blood flow with hydrogen gas. Circ. Res. 1964; 14:164–187. [PubMed: 14118761]
22. Fellows LK, Boutelle MG. Rapid changes in extracellular glucose levels and blood flow in the striatum of the freely moving rat. Brain Res. 1993; 604:225–231. [PubMed: 8457850]
23. Lowry JP, Boutelle MG, Fillenz M. Measurement of brain tissue oxygen at a carbon paste electrode can serve as an index of increases in regional cerebral blood flow. J. Neurosci. Methods. 1997; 71:177–182. [PubMed: 9128153]
24. Stosseck K, Lübbers DW, Cottin N. Determination of local blood flow (microflow) by electrochemically generated hydrogen. Pflügers Archiv. 1974; 348:225–238. [PubMed: 4857963]
25. Young W. H2 clearance measurement of blood flow: a review of technique and polarographic principles. Stroke. 1980; 11:552–564. [PubMed: 6999671]
26. Meyer JS, Fukuuchi Y, Kanda T, Shimazu K, Hashi K. Regional cerebral blood flow measured by intracarotid injection of hydrogen Comparison of regional vasomotor capacitance from cerebral infarction versus compression. Neurology. 1972; 22:571–571. [PubMed: 4628339]

27. Koshu K, Kamiyama K, Oka N, Endo S, Takaku A, Saito T. Measurement of regional blood flow using hydrogen gas generated by electrolysis. Stroke. 1982; 13:483–487. [PubMed: 7101348]
28. Dengler AK, McCarty GS. Microfabricated microelectrode sensor for measuring background and slowly changing dopamine concentrations. J. Electroanal. Chem. 2013; 693:28–33.
29. Shin JH, Privett BJ, Kita JM, Wightman RM, Schoenfisch MH. Fluorinated xerogel-derived microelectrodes for amperometric nitric oxide sensing. Anal. Chem. 2008; 80:6850–6859. [PubMed: 18714964]
30. Hu F, Karweik DH, Kuwana T. Activation and deactivation of glassy carbon electrodes. J. Electroanal. Chem. Interfacial Electrochem. 1985; 188:59–72.
31. Hawley M, Tatawawadi S, Piekarski S, Adams R. Electrochemical studies of the oxidation pathways of catecholamines. J. Am. Chem. Soc. 1967; 89:447–450. [PubMed: 6031636]
32. Macpherson JV, Unwin PR. Determination of the diffusion coefficient of hydrogen in aqueous solution using single and double potential step chronoamperometry at a disk ultramicroelectrode. Anal. Chem. 1997; 69:2063–2069. [PubMed: 21639247]
33. Chen Y-Y, Lai H-Y, Lin S-H, Cho C-W, Chao W-H, Liao C-H, et al. Design and fabrication of a polyimide-based microelectrode array: application in neural recording and repeatable electrolytic lesion in rat brain. J. Neurosci. Methods. 2009; 182:6–16. [PubMed: 19467262]
34. Fernández D, Maurer P, Martine M, Coey J, Möbius ME. Bubble formation at a gas-evolving microelectrode. Langmuir. 2014; 30:13065–13074. [PubMed: 24694174]
35. Macpherson JV, O'Hare D, Unwin PR, Winlove CP. Quantitative spatially resolved measurements of mass transfer through laryngeal cartilage. Biophys. J. 1997; 73:2771. [PubMed: 9370471]
36. Bard, AJ.; Faulkner, LR.; Leddy, J.; Zoski, CG. Electrochemical methods: fundamentals and applications. Vol. 2. New York: Wiley; 1980.
37. Robinson J, Cooper JM. Method of determining oxygen concentrations in biological media, suitable for calibration of the oxygen electrode. Anal. Biochem. 1970; 33:390–399. [PubMed: 4314758]
38. Ndubuizu O, LaManna JC. Brain tissue oxygen concentration measurements. Antioxid. Redox Signal. 2007; 9:1207–1220. [PubMed: 17536959]
39. Feng Z-C, Roberts EL, Sick TJ, Rosenthal M. Depth profile of local oxygen tension and blood flow in rat cerebral cortex, white matter and hippocampus. Brain Res. 1988; 445:280–288. [PubMed: 3130957]
40. Sugawara Y, Okayasu T, Yadav AP, Nishikata A, Tsuru T. Dissolution mechanism of platinum in sulfuric acid solution. J. Electrochem. Soc. 2012; 159:F779–F786.
41. Klein B, Kuschinsky W, Schrock H, Vetterlein F. Interdependency of local capillary density, blood flow, and metabolism in rat brains. Am. J. Physiol. Heart Circ. Physiol. 1986; 251:H1333–H1340.
42. Fieschi C, Bozzao L, Agnoli A. Regional clearance of hydrogen as a measure of cerebral blood flow. Acta Neurol. Scand. 1965; 41:46–52.
43. Ciolkowski EL, Cooper BR, Jankowski JA, Jorgenson JW, Wightman RM. Direct observation of epinephrine and norepinephrine cosecretion from individual adrenal medullary chromaffin cells. J. Am. Chem. Soc. 1992; 114:2815–2821.
44. Sakurada O, Kennedy C, Jehle J, Brown J, Carbin GL, Sokoloff L. Measurement of local cerebral blood flow with iodo [14C] antipyrine. Am. J. Physiol. Heart Circ. Physiol. 1978; 234:H59–H66.
45. Hawley MD, Feldberg SW. Nuances of the ECE Mechanism. I. Development of the Theoretical Relationships for Chronoamperometry1a. J. Phys. Chem. 1966; 70:3459–3464.
46. Takmakov P, Zachek MK, Keithley RB, Walsh PL, Donley C, McCarty GS, et al. Carbon microelectrodes with a renewable surface. Anal. Chem. 2010; 82:2020–2028. [PubMed: 20146453]

Highlights

- An electrolytic hydrogen clearance sensor is microfabricated and characterized.
- Micron-scale dimensions enhance the technique's temporal and spatial resolution.
- Computational modeling anticipates deviations from ideal sensor performance.
- Sensors are sensitive to physiologically expected cerebral blood flow rates.
- Low-noise systems improve accuracy and electrode cycling ensures reproducibility.

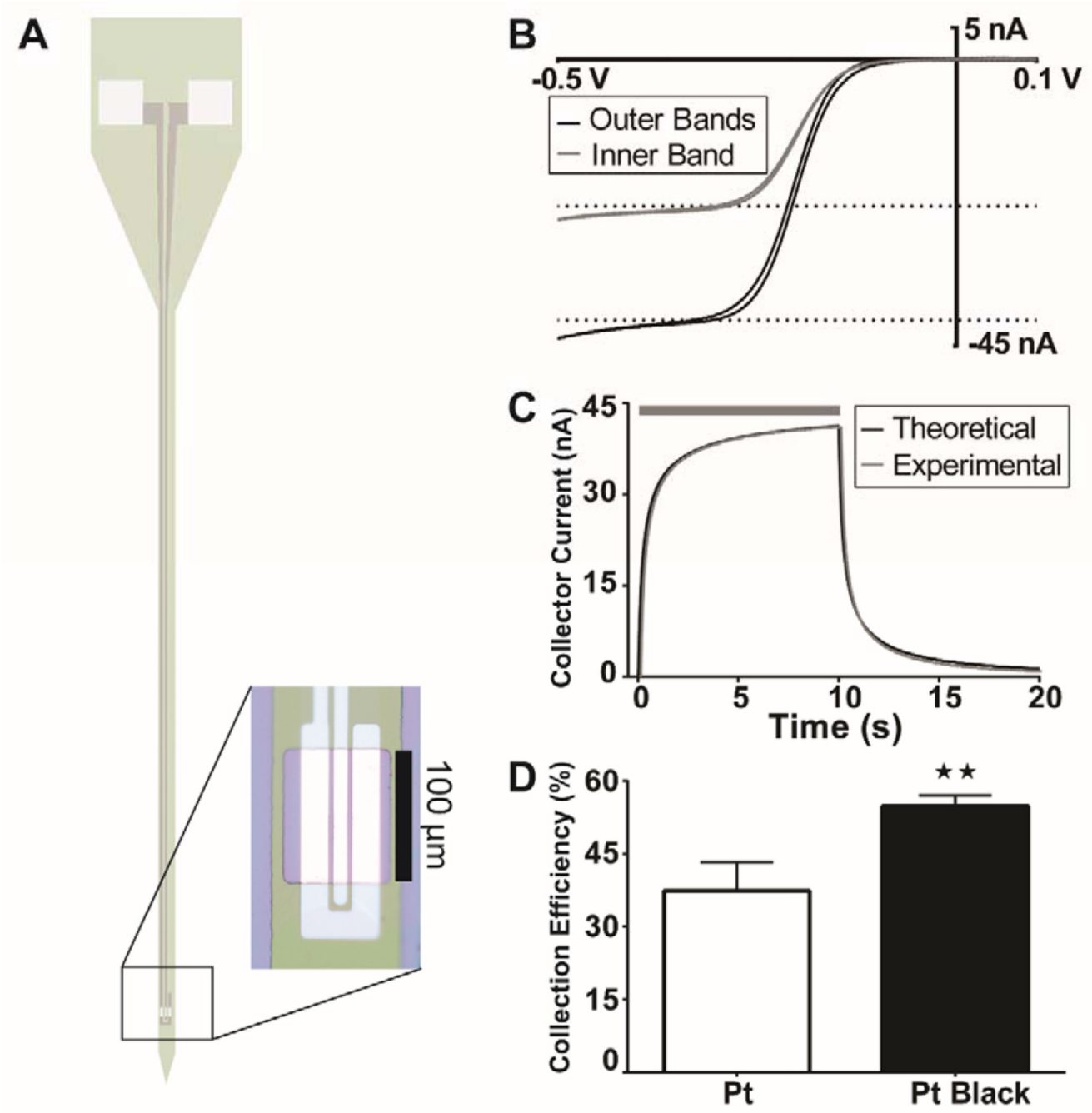

Figure 1.

Microfabricated platinum arrays are characterized by voltammetry and amperometry. (A) Model (to scale) of the full device shows two separately addressed, 100 µm long electrodes (inset: micrograph) selectively exposed at the tip. Inset color key: Purple is exposed silicon, green is silicon nitride, grey is insulated platinum beneath the nitride and white is bare platinum. (B) Cyclic voltammogram (5 mV s^{-1}) in degassed solution containing 2.5 mM RuHex and 0.1 M KCl. Theoretical steady state currents, indicated as dashed lines, were used to confirm active electrode surface areas. (C) Clearance curves obtained from

generating RuHex (II) (35 mM) in the period indicated by the grey bar, and collecting RuHex (III). Outer electrodes used −100 nA pulses to reduce RuHex (III). The inner electrode, held at +0.25 V, detects RuHex (II) oxidation as faradaic current. Experimental RuHex clearance shows excellent agreement with simulations of the same system. (D) The collection efficiencies, taken at the plateau current, significantly increases when all electrodes are electroplated in platinum black (Student's *t*-test: $t_{(2,6)} = 4.804$, $P = 0.003$).

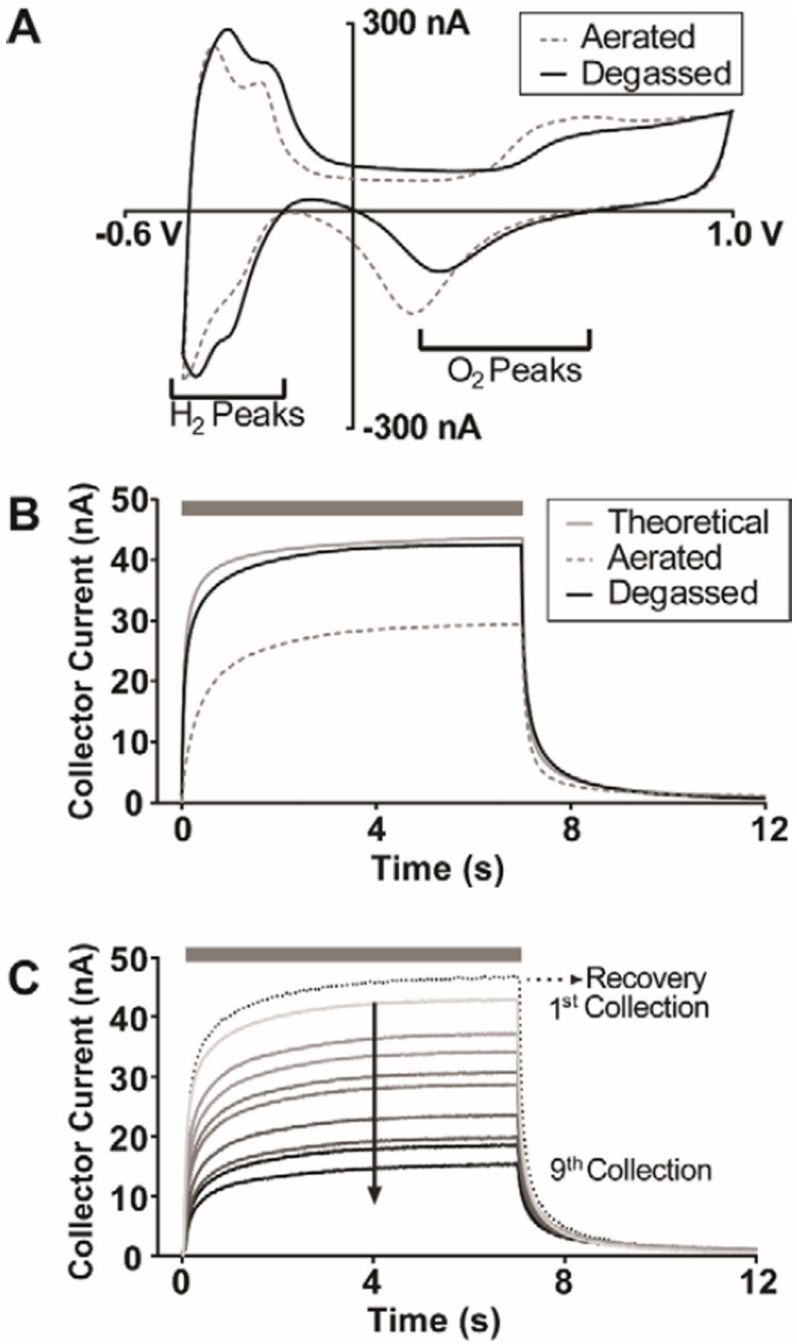

Figure 2.

O_2 reduction reactions compete with EHC in 0.5 M H_2SO_4 at bare Pt electrodes. (A) Steady-state cyclic voltammograms (inner electrode shown, 20 V s^{-1}) indicate augmented H_2-adsorption peaks at a platinum surface in degassed acid versus air-saturated acid. In degassed solution, the decreased area beneath the O_2 adsorption-desorption peaks also presents with a potential shift of the cathodic peak, indicative of fewer oxides present at the surface. (B) EHC curves in 0.5 M H_2SO_4 indicate that CE decreases in air-saturated solutions, but can be restored to theoretical levels after N_2 bubbling. (C) Even EHC in

degassed H_2SO_4 is subject to CE deterioration between subsequent pulses. Cycling the collector between pulses recovers CE (clearance curve indicated by dotted arrow) and ensures a maximized, consistent response. Generator pulses used were −100 nA. Collector potentials were held at +0.25 V.

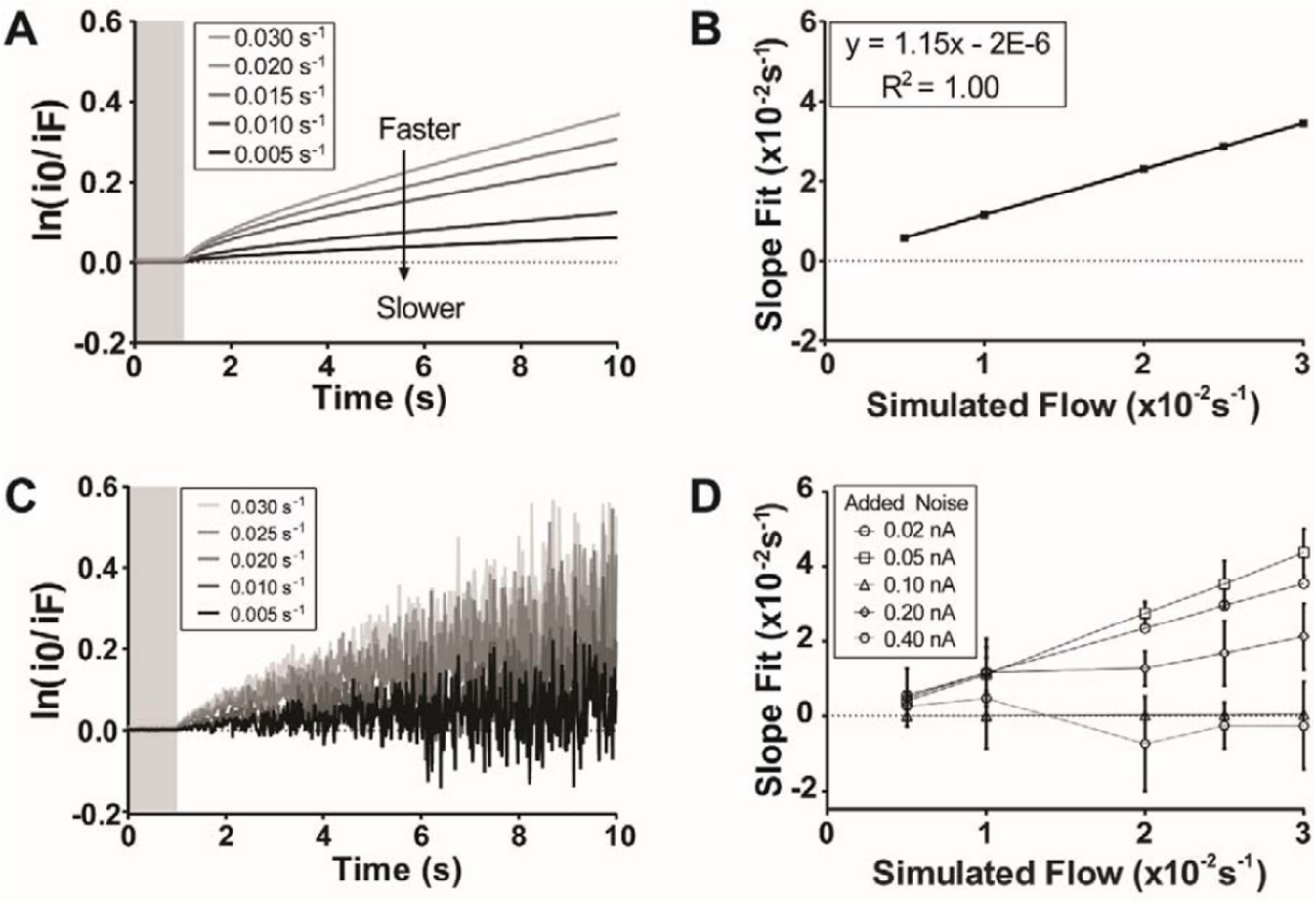

Figure 3.

Computer modeling using COMSOL predicted experimental inaccuracies. (A) Simulated clearance curves for a range of physiologically expected flow rates were calculated and plotted following analysis with Equation 19. Time = 0 indicates the cessation of the generating pulse. The first second of clearance (shaded box) is excluded from the linear regression fit. (B) The linear fit slopes from plot A were compared to the actual rates used in the model. The calculated fits overestimated the true rate, but in a highly predictable manner amenable to correction. (C) The data from A with added Gaussian noise (0.02 nA). (D) Linear fits from C data with greater noise amplitudes can be less accurate at predicting the true microflow values. N = 4 replicates per noise value, per flow. Error bars ± S.D.

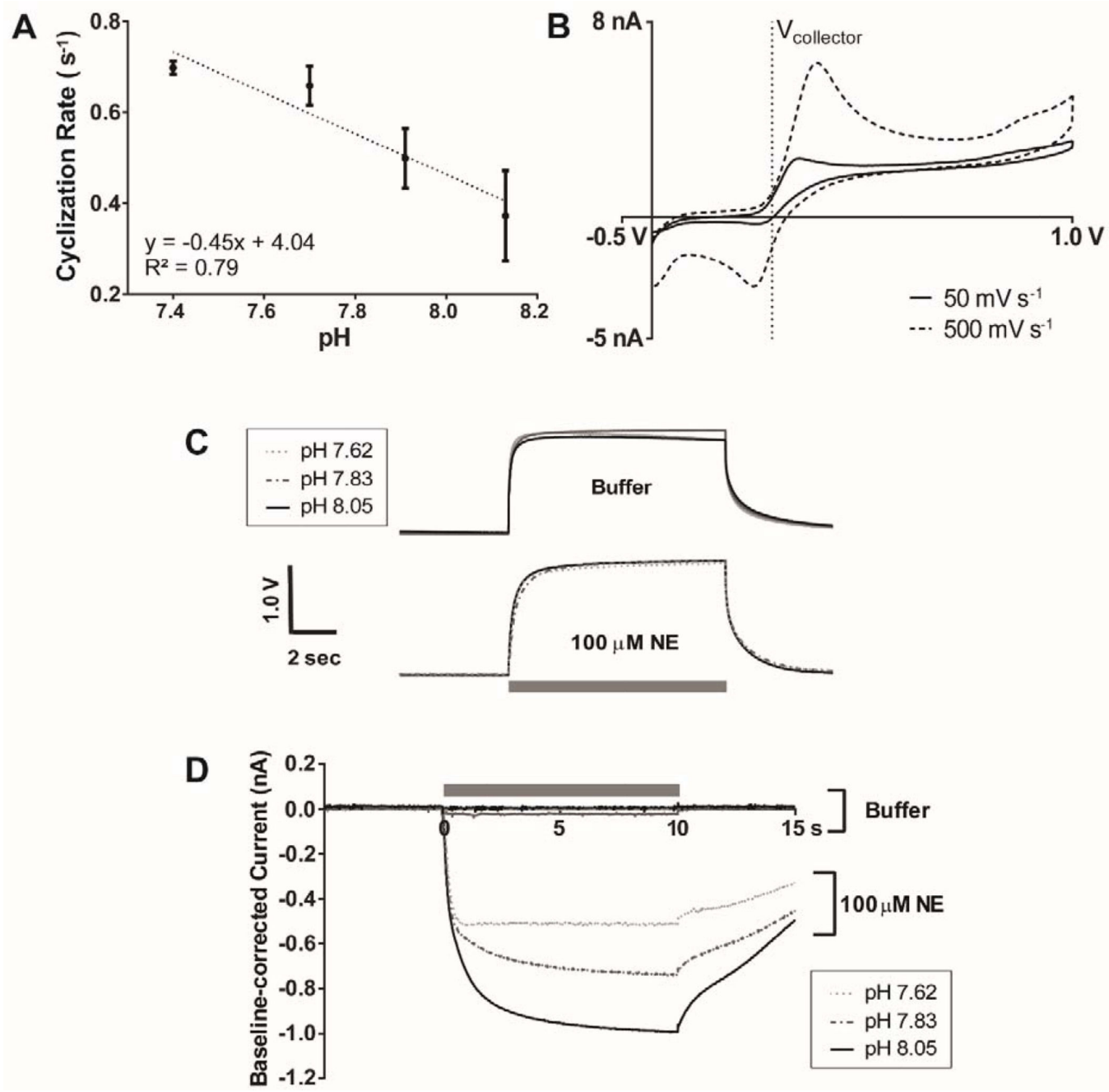

Figure 4.

The intracyclization rate of NE-orthoquinone was used to model a first order reaction decay in lieu of perfusion experiments. (A) The rate of the reaction was determined in solutions of varying pH using potential-step amperometry at a glassy carbon disk electrode (n = 4 replicates). (B) Cyclic voltammetry performed in 100 μM NE solutions was used to select a collector potential, $V_{Collector}$ = 0.0 V, to detect Peak 1, NE, and exclude faradaic currents from Peak 2, leuco-noradrenochrome. (C) Representative voltage vs. time traces at the generator electrode producing a 10 s, +100 nA pulse. NE oxidation significantly raised the voltages necessary to produce a generating pulse against buffer alone (1.59 ± 0.002 from

1.45 ± 0.01 V, $t_{(2,4)}$ = 9.262, P = 0.0008). (D) Representative current vs. time plots with the collector held at 0.0 V during a 10 s, +100 nA pulse. In solutions with NE, the collector was capable of detecting Peak 1 from B across all pH values tested (n = 11 replicates). Grey bars indicate pulse time.

TABLE 1

EHC collection efficiencies measured at bare platinum arrays using the center electrode as the collector and two outer bands as generators. Collection efficiency reported at the end of a 7 s generation of H_2.

Solution	Pulse Amplitude (nA)	Collection Efficiency (%)[a]
Modeled Prediction	−100	43.6
Aerated H_2SO_4	−100	25.2 ± 3.0 ***
Degassed H_2SO_4	−100	34.6 ± 5.9
Aerated PBS	−100	n/a[b]
	−700	0.49 ± 0.18 ****
Degassed PBS	−100	30.4 ± 7.4

[a] Presented as averages ± S.D. Significance calculated using Student's *t*-test and Welch's correction against theoretical values: ***$P < 0.001$, ****$P < 0.0001$.

[b] Generating current used was insufficient to produce a collector response above baseline.